AIAA 2006-2887

Skin Friction and the Inner Flow in Pressure Gradient Turbulent Boundary Layers

Katherine Newhall, Brian Brzek, Raúl Bayoán Cal,
Gunnar Johansson, and Luciano Castillo

36th Fluid Dynamics Conference & Exhibit
June 5–8, 2006/San Francisco, CA

Skin Friction and the Inner Flow in Pressure Gradient Turbulent Boundary Layers

Katherine Newhall*, Brian Brzek†, Raúl Bayoán Cal‡, Gunnar Johansson§, and Luciano Castillo¶

Abstract

This investigation will look at multiple methods to determine the wall shear stress for several pressure gradient turbulent boundary layer flows, particularly favorable pressure gradient and zero pressure gradient. These methods include using the slope at the wall, the integrated bounary layer equation, momentum integral equation and the Clauser method. In order to perform this study, 2D Laser Doppler Anemometry, (LDA), measurements of the velocity field near the wall for various streamwise positions have been carried out at the Chalmers L2 wind-tunnel. With the resulting wall shear stress calculations, the effects of pressure gradient and upstream conditions will be investigated on the inner region of the velocity profiles and Reynolds stresses. As will be seen, the integrated boundary layer equation is the most accurate technique to determine the wall shear stress when direct measurements are not available. In addition, the velocity profiles show a mild effect of the pressure gradient. The Reynolds stresses show a large effect of the pressure gradient in inner variables, but not below, $y^+ < 30$. The shape of the Reynolds stresses $< v^2 >$ and $< uv >$ components changes significantly due to the external pressure gradient, damping them as much as 40%, though the streamwise $< u^2 >$ component exhibits an insignificant amount of change.

Introduction

The effects of Reynolds number and pressure gradient on the skin friction coefficient, C_f, and the velocity field have long been debated as well as the accuracy of various techniques used to determine this quantity. Some of the more common methods to obtain the skin friction include direct measurements such as oil-film interferometry, force balance and the newer MEMS devices. Common velocity based methods include computing the slope at the wall and evaluating the momentum equation. Various in-direct measurements such as the Clauser method and Preston total head tubes are also used. Many of the theories and methods have been proven valid for the ZPG boundary layer, in various ranges of Reynolds number. However, these theories become more complex in the presence of an external pressure gradient.

Accurate values of C_f are of particular importance due to its direct relationship to u_*, the friction velocity. Through similarity analysis, George and Castillo (1997) found that the friction velocity is the correct velocity scale for the inner region of the boundary layer. Also, the inner similarity length scale involves u_* and the Reynolds stress inner similarity scale is u_*^2. Accurate values of the friction velocity are needed to view profiles in inner similarity variables. Also, obtaining accurate values of C_f will enable better predictions of the friction drag for airplanes, submarines, and ships. With knowledge of the behavior of the skin friction coefficient under a variety of flow conditions, different ideas can be implemented for drag reduction studies.

To aid in determining accurate values of the skin friction, this investigation will evaluate different techniques in terms of their accuracy and limitations. Also, the effects of an external pressure gradient on the skin friction, as well as the scaled velocity profiles and Reynolds stresses in inner variables will be examined.

Experimental Setup

This analytical study will look at four methods to calculate the wall shear stress for different pressure gradient turbulent boundary layer flows. Specifically, the investigation will use the ZPG data of Castillo/Johansson (CJ) (2002) as well as the developing FPG flow of Cal et al. (2005). Both of these experiments were performed in the Chalmers University of Technology L2 wind-tunnel, where upstream conditions such as wind-tunnel speed and trip wire size and location could be controlled. The wind-tunnel has a test section that is 3 m long, 1.8 m wide and 1.3 m high and is a closed loop design.

In each case, the flat plate was installed vertically in the wind-tunnel and various wind-tunnel speeds were

*MS, Rensselaer Polytechnic Institute, Department of Mechanical, Aeronautical and Nuclear Engineering, Troy, NY 12180

†PhD, Rensselaer Polytechnic Institute, Department of Mechanical, Aeronautical and Nuclear Engineering, Troy, NY 12180

‡Post-doctoral fellow, The Johns Hopkins University, Department of Mechanical Engineering, Baltimore, MD

§Associate Professor, Chalmers Institute of Technology, Gothenburg, Sweden

¶Associate Professor, Rensselaer Polytechnic Institute, Department of Mechanical, Aeronautical and Nuclear Engineering, Troy, NY 12180, also Research Professor at University of Puerto Rico-, Mayagüez, Mayagüez, P.R., Department of Mechanical Eng.

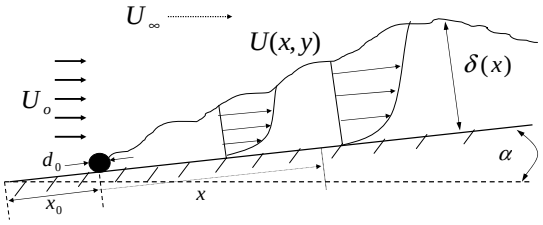

Fig. 1 Schematic of favorable pressure gradient boundary layer

used. Upstream wind-tunnel speeds of 4.6 and 8.4 m/s were used for the FPG experiment, whereas 5, 10 and 20 m/s were used in the ZPG experiment of CJ. For the FPG case the flat plate was tilted at various angles to create variable pressure gradient strengths. The plate angles of 3.5 (S-FPG 1 and 2) and 7 (S-FPG 3) degrees resulted in weak developing FPG flows. These flows begin as ZPG flows and slowly accelerate down the plate. The strongest pressure gradient (S-FPG 4) is created with a plate angle of 15 degrees. A schematic of the set up appears in figure 1. Reynolds numbers based on momentum thickness between 760 and 5300 are achieved for the different cases and appear with other external conditions in table 1.

Two LDA probes with a measuring control volume of $58\mu m$ in diameter were used and measurements as close to the wall as $y^+ \approx 2$ for the ZPG experiment and $y^+ \approx 4$ for the FPG experiment were achieved. A complete description of the LDA system can be found in Castillo and Johansson (2002) or in Cal et al. (2005) which includes more information about the system. For each set of external conditions, measurements were taken at 12 downstream locations to obtain accurate information about changes in the streamwise direction. Table 1 contains the test matrix for all experiments giving the upstream wind-tunnel speed, plate angle and range of Reynolds numbers.

Flow	U_o(m/s)	Angle(deg)	Re_θ Range
S-CJ 1	4.9	0	760 → 1600
S-CJ 2	10.0	0	1500 → 3000
S-CJ 3	20.0	0	4200 → 5300
S-FPG 1	8.4	3.5	1300 → 2100
S-FPG 2	4.6	3.5	680 → 1200
S-FPG 3	8.4	7	1100 → 1800
S-FPG 4	10.0	15	1200 → 1700
Österlund	40	0	2500 → 6400
Smith-Smits	33	0	1170 → 2800

Table 1 Experimental Conditions

Inner Scaling

George and Castillo (1997) determined the scalings for the inner boundary layer equations for a zero pressure gradient boundary layer using similarity analysis. This was extended to boundary layers subjected to pressure gradients by Castillo and George (2001). Similarity solutions for the mean velocity and Reynolds stresses for the inner flow are assumed to be the product of two functions,

$$U = U_{si}(x) f_i(y^+, \delta^+, \lambda^+, *) \tag{1}$$

$$- < uv >= R_{si_{uv}}(x) r_i(y^+, \delta^+, \lambda^+, *) \tag{2}$$

$$< u^2 >= R_{si_{u^2}}(x) k_{ui}(y^+, \delta^+, \lambda^+, *) \tag{3}$$

$$< v^2 >= R_{si_{v^2}}(x) k_{vi}(y^+, \delta^+, \lambda^+, *) \tag{4}$$

where λ^+ is the dependence on the pressure gradient. In the product solution, U_{si} and $R_{si_{uv}}$ are the inner velocity scale and the inner Reynolds shear stress scale respectively and depend on x only. The scales for the inner Reynolds normal stresses are given by $R_{si_{u^2}}$ and $R_{si_{v^2}}$ and also depend on x. These are unknown scales at this moment and will be determined strictly by the similarity analysis of the equations of motion. The similarity functions in inner scaling are given by f_i, r_i, k_{ui} and k_{vi}. The dependent variables of the similarity solutions are $y^+ = yu_*/\nu$, the inner similarity length scale, the local Reynolds number dependence, $\delta^+ = \delta u_*/\nu$, the pressure gradient, $\lambda^+ = (\nu/\rho u_*^3) dP_\infty/dx$ and any possible dependence on the upstream conditions, *, respectively.

In the inner region of the flow the boundary layer equations reduce to,

$$0 = \frac{-1}{\rho}\frac{dP_\infty}{dx} + \frac{\partial}{\partial y}\left[- < uv > + \nu \frac{\partial U}{\partial y} \right], \tag{5}$$

where the pressure gradient term is maintained since it can not necessarily be neglected before hand. The Reynolds stresses have been neglected since they are small in comparison to the other terms in equation 5. Integrating equation 5 from $y' = 0$ to $y' = y$ and using the fact that $U =< uv >= 0$ at $y = 0$ and that $\nu \left.\frac{\partial \overline{U}}{\partial y}\right|_{y=0} = u_*^2$ results in:

$$\frac{\tau_w}{\rho} = u_*^2 = -\frac{y}{\rho}\frac{dP_\infty}{dx} - < uv > + \nu \frac{\partial U}{\partial y} \tag{6}$$

Substituting equations 1 to 4 into equation 6, the resulting scalings can be determined. With the correct choice of scales, all the terms maintain the same relative balance as the flow develops in the streamwise direction. Consequently, it can be shown that in inner variables, the velocity profiles should be scaled with the friction velocity, $U_{si} \sim u_*$ and all components of the Reynolds stresses should also be scaled with the friction velocity squared, $R_{si_{u^2}} \sim R_{si_{v^2}} \sim R_{si_{uv}} \sim u_*^2$ as in the classical theory if the pressure gradient is assumed to not influence the scalings.

Using these scalings, equation 6 is transformed into

$$1 = -\frac{y^+ \nu}{\rho u_*^3}\frac{dP_\infty}{dx} - \frac{< uv >}{u_*^2} + \frac{\nu}{u_*^2}\frac{\partial U}{\partial y}. \tag{7}$$

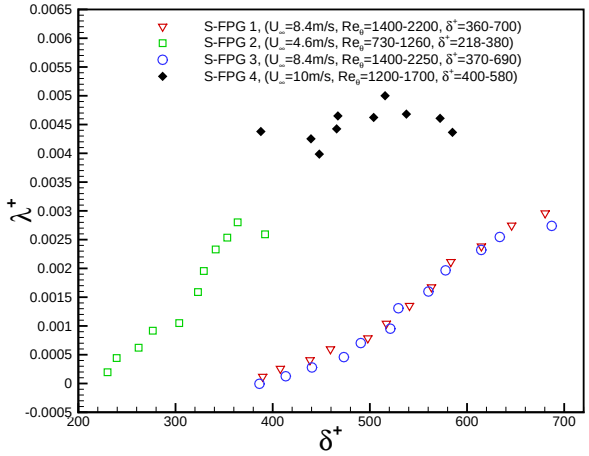

a) λ^+ vs δ^+ for the FPG experiment of Cal(2005)

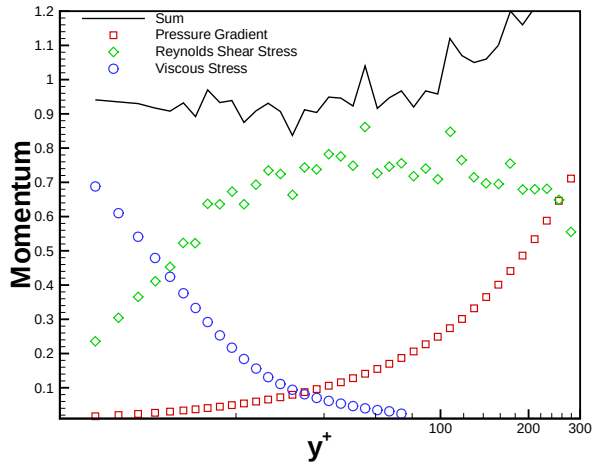

b) Momentum equation in inner variables

Fig. 2 Inner momentum equation

Retaining the pressure gradient term, equation 7 can be written in terms of the inner scalings as

$$1 = -y^+\lambda^+ - r_i + f_i', \tag{8}$$

the inner similarity boundary layer equation, where $\lambda^+ = \frac{\nu}{\rho u_*^3}\frac{dP_\infty}{dx}$, $r_i = \frac{<uv>}{u_*^2}$ and $f_i' = \frac{\partial U^+}{\partial y^+} = \frac{\nu}{u_*^2}\frac{\partial U}{\partial y}$. As $\lambda^+ \to \infty$, the pressure gradient increases, and when $\lambda^+ = 0$, the flow is considered to be a zero pressure gradient flow.

The pressure gradient for the four FPG experiments are shown in inner variables (i.e., λ^+ vs δ^+) in Figure 2(a). In each case, λ^+ increases in the downstream direction indicating the nature of the developing FPG flow. In addition, the balance of equation 7 is plotted in figure 2 for one location ($\delta^+ = 630$) of the S-FPG 3 flow (7^o plate angle). The line indicating the sum of the terms is flat, except for fluctuations due to measurement error, indicating that equation 7 holds up to $y^+ \approx 100$. The sum of the terms is not exactly 1, which can be attributed to the difficulty of attaining an accurate value of the friction velocity, u_*, used to scale each term. Notice that the pressure gradient term involving λ^+ contributes 5% at $y^+ \approx 20$ and increases rapidly. By $y^+ \approx 100$ the balance of equation 7 breaks down, since the mean convection terms which are small and negligible in the inner region, begin to play a role in the momentum balance. It is important to note that for this particular profile, $y/\delta_{95} = 0.1$ occurs at $y^+ = 67$, thus showing the slow turn on of the mean convection terms.

Skin Friction

The other methods for determining the skin friction will be compared to the more accurate method of direct measurement with oil film interferometry technique. Since oil film values for the specific cases involved is not available, the curve fit of Österlund is used. For a zero pressure gradient boundary layer, the curve

$$C_f = 2\left[\frac{1}{\kappa}\ln(Re_\theta) + C\right]^{-2}, \tag{9}$$

where κ is 0.384 and C is 4.08 is used to determine the skin friction. This correlation is considered to be "exact", so it is used to evaluate the accuracy of the other methods for determining skin friction on smooth zero pressure gradient flows.

Boundary Layer Equation

The integrated boundary layer equation given by equation 10 is obtained by integrating the mean momentum equation and using the continuity equation for the normal velocity, V. In addition, a correction for the pressure gradient across the boundary layer is incorporated using the wall normal Reynolds stress component, $< v^2 >$, by integrating the wall normal momentum equation for the pressure. Often times the gradient terms of the Reynolds stresses are ignored since they are small, but they are kept here as they account for approximately 3% and 2% percent of the total, for the u and v components respectively. The boundary layer equation is integrated from $y' = 0$ to $y' = y$ for the flow over a flat plate, subject to an external pressure gradient.

$$\frac{\tau_w}{\rho} = u_*^2 = \underbrace{\nu\frac{\partial \overline{U}}{\partial y}}_{(1)} \underbrace{-\overline{uv} - \int_0^y \frac{\partial \overline{U}^2}{\partial x}dy' + \overline{U}\int_0^y \frac{\partial \overline{U}}{\partial x}dy'}_{(3)} - \int_0^y \frac{\partial \overline{u^2}}{\partial x}dy' + \int_0^y \frac{\partial \overline{v^2}}{\partial x}dy' + \underbrace{U_\infty \frac{dU_\infty}{dx}y}_{(6)}, \tag{10}$$

Johansson/Castillo (2002) demonstrated that the pressure gradient term (term 6) must be included even for zero pressure gradient flows, as it is nearly impossible to obtain a completely uniform velocity distribution along the entire surface. Even a small pressure

gradient is important in the outer region of the boundary layer, since this term is multiplied by the wall normal coordinate, y. Notice that any error in this term is also amplified in the outer region.

Observe that in equation 10, the wall shear stress is related to the friction velocity and in this form of the equation knowledge of the x-dependence of the velocity field is required. Throughout the entire boundary layer the shear stress on the left hand side is constant; therefore at any y-location the sum of all the terms on the right hand side should also be constant. Furthermore, to obtain a single value for the skin friction, the individual total values at each y-location are averaged from $y/\delta = 0.2$ to $y/\delta = 0.8$. This averages out the noise while excluding the near wall region where the fluctuations are largest. It also excludes the exterior of the boundary layer where errors in the pressure gradient term, $U_\infty \frac{dU_\infty}{dx} y$, are amplified. This technique to obtain the value of the skin friction is referred to as the "integrated boundary layer" technique.

In the limit as $y \to \infty$, equation 10 reduces to the momentum integral equation,

$$\frac{\tau_w}{\rho} = u_*^2 = U_\infty^2 \frac{d\theta}{dx} + \left(2 + \frac{\delta_*}{\theta}\right) U_\infty \theta \frac{dU_\infty}{dx}, \qquad (11)$$

after substituting the definitions of δ_* and θ. When using the momentum integral equation, the derivatives $d\theta/dx$, and dU_∞/dx must be determined experimentally, which is not trivial. In order to reduce the error in computing the derivative of θ, accurate near wall measurements are required and a high resolution of data points in the outer flow are needed (Johansson/Castillo 2002) because changes in momentum thickness occur in the outer flow. In addition, to accurately compute the derivatives many downstream positions must be considered. The same is true for the displacement thickness. The integrand is largest between $y = 0$ and the first actual measured point. Therefore accurate near wall measurements are required to accurately determine these parameters.

The derivatives in equation 11 must be determined empirically and is further complicated by complex pressure gradients. To compute the derivatives, multiple curve fits including various order polynomials and power laws are used. For each type of fit, the skin friction coefficient is computed and the results are averaged. In general, the fits deviate at the first and last measurement locations, creating errors in the derivatives at these points, and therefore errors in the skin friction. In general, this method should be applied to interior locations, with one or more other measurement locations on either side. This technique to obtain skin friction measurements is referred to as the "momentum integral equation".

Slope at the Wall

The slope at the wall technique is another velocity based technique considered to be exact. Limitations

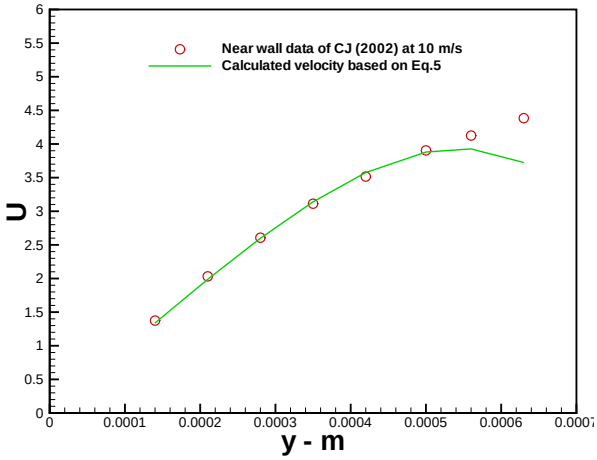

Fig. 3 Theoretical near wall velocity profile

arise from determining the mean velocity such as probe size resolution issues and locating the wall. Near the wall, the velocity is given by

$$\overline{U} = y \left.\frac{\partial \overline{U}}{\partial y}\right|_{y=0} - \frac{y^2}{2} \left.\frac{\partial^2 \overline{U}}{\partial y^2}\right|_{y=0} + \frac{y^4}{24} \left.\frac{\partial^4 \overline{U}}{\partial y^4}\right|_{y=0} + O(y^5). \qquad (12)$$

The second derivative term arises from the pressure gradient and it can be demonstrated that the third order term is zero, even for flows with pressure gradient. This equation is not limited to the linear sublayer. Johansson/Castillo (2002) found it to be valid up to $y^+ \approx 10$.

The evaluation of equation 12 requires the determination of $\frac{\partial \overline{U}}{\partial y}$, $\frac{\partial^2 \overline{U}}{\partial y^2}$ and $\frac{\partial^4 \overline{U}}{\partial y^4}$ evaluated at $y = 0$, the location of the wall. This can be accomplished by fitting a polynomial of the form,

$$\overline{U_f} = a(y - y_0) - \frac{1}{2\nu} U_\infty \frac{dU_\infty}{dx} (y - y_0)^2 + b(y - y_0)^4, \qquad (13)$$

to the measured mean velocity data near the wall. An adjustment to the wall location, y_0, is included in equation 13. This wall adjustment has been fixed at zero for the data considered here, since its value is known to be small in comparison to the first y location.

Least squares optimization was used to determine the coefficients a and b in equation 13. With the known coefficients, the wall shear stress can be computed by

$$\frac{\tau_w}{\rho} = a\nu. \qquad (14)$$

The computed velocity profile near the wall is plotted in figure 3. The departure of equation 13 from the experimental data occurs at approximately 0.5mm, or $y^+ \approx 13$.

One of the drawbacks of using this technique is that it relies on accurate measurements in the near wall region ($y^+ < 2$) which is challenging. This method is also limited by the ability to identify the exact y-location of the wall. LDA measurements have inherent

error due to velocity biasing and positioning errors near the wall, Johansson/Castillo (2002).

The Clauser Method

Using the Clauser (1954) method to determine the skin friction has been the traditional approach used for the past 70 years. This is accomplished by plotting the profiles of $\frac{U}{u_*}$ vs. $\frac{yu_*}{\nu}$ in semi-log scale and then optimizing the function

$$\frac{U}{u_*} = \frac{1}{\kappa} \ln\left(\frac{yu_*}{\nu}\right) + B \qquad (15)$$

until it matches the data in the overlap region. For this method κ and B are universal constants whose exact values are argued over by many researchers. Traditionally, values of $\kappa = 0.41$ and $B = 5.25$ have been used. These values are used in the present study. However, many experiments have shown the value to be closer to 0.38 or 0.39, and Nagib et al. (2005) has shown that the value of κ may depend on the strength of the pressure gradient, while others have shown it depends on Reynolds number.

The Clauser method is based on the fact that a logarithmic region exists in the overlap region. Fernholz and Warnack (1998) showed that as the favorable pressure gradient increases, the overlap region narrows until it no longer exists. With few or no points to fit, the Clauser method is difficult or impossible to implement. Consequently, other methods are needed to accurately determine the wall shear stress for these flows.

Results

The Skin Friction Coefficient

The values of C_f obtained from the four methods discussed above, integrated boundary layer equation 10, momentum integral equation 11, slope at the wall equation 14 and the Clauser technique are plotted in figure 4(a) along with the Österlund correlation (equation 9), for the zero pressure gradient data sets S-CJ 1 and S-CJ 2.

Near wall measurements are needed for the slope at the wall technique to perform well. At a wind-tunnel speed of 5 m/s, measurements down to $y^+ \approx 2$ were obtained for S-CJ 1. Therefore, the slope at the wall technique nearly matches the Österlund correlation with an error of $3-6\%$. However, for the experimental data at 10 m/s, with measurements down to $y^+ \approx 4$, the slope at the wall technique under predicts the skin friction coefficient by about $10-15\%$ when compared to the Österlund correlation.

The momentum integral equation 11, tends to over predict the skin friction (figure 4(a)) for the zero pressure gradient 10 m/s data, for the majority of the profiles. The values obtained from the integrated boundary layer equation 10 match the exact result on average, however a few points have large error.

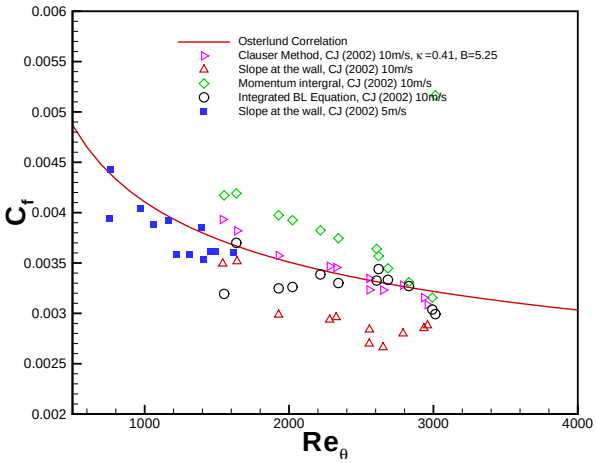

a) C_f results for the data of CJ (2002) at 10m/s

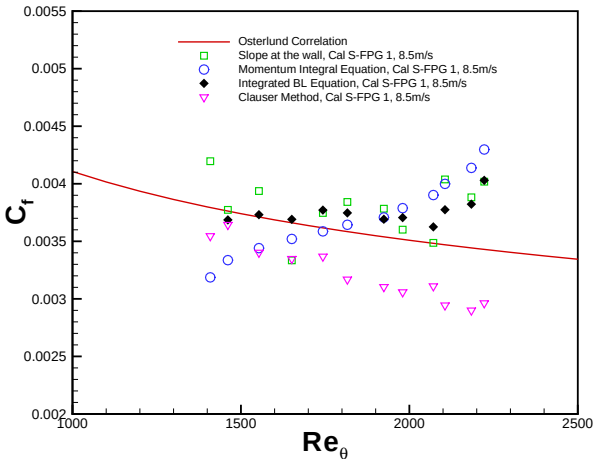

b) C_f results for the data of Cal et al.(2005) at 10m/s

Fig. 4 Skin friction measurements

These two techniques use different forms of the same equation, and yield different results, showing their sensitivity to different parts of the flow and sources of error. It is known that near wall measurements were hard to obtain for S-CJ 2, therefore indicating that the momentum integral equation is more sensitive to the near wall region than the integrated boundary layer equation. The integrated boundary layer equation is expected to yield more accurate results on a larger range of different flows.

The addition of the external pressure gradient (Cal 2005) complicated the methods to determine skin friction and the evaluation of the accuracy of these methods. Given the inability to resolve the current oil film interferometry measurements, the methods used to compute the skin friction do not have a direct basis for which to compare. Since S-FPG 1 is known to be a mild favorable pressure gradient, the first few downstream locations can be approximated by having no pressure gradient. The skin friction values obtained from the four methods are plotted in figure 4(b) along with the Österlund correlation as a bench mark.

It is known that as the mild pressure gradient increases, the skin friction should also increase. The values obtained by the Clauser method do not exhibit this trend, remaining significantly below the Österlund correlation. These values differ from the integrated boundary layer equation values by as much as 25%. The slope at the wall technique exhibits the proper trend, yet there is some scatter, more than the integrated boundary layer equation values. Measurements were obtained down to $y^+ \approx 4$. Since the values of skin friction are scattered here and not when measurements were obtained down to $y^+ \approx 2$, the slope at the wall method will be ineffective if measurements are not taken down to at least $y^+ \approx 4$. The momentum integral equation 11 yielded an overall increasing trend to the skin friction values, which is not expected in the first few downstream locations, since the flow is basically a zero pressure gradient. The integrated boundary layer equation 10 is the most accurate. The values obtained from this method follow the zero pressure gradient correlation for the first few downstream locations, then depart and increase as the pressure gradient increases. There is also very little scatter in this method as compared to the slope at the wall method.

The integrated boundary layer equation technique works the best for the FPG flow considered compared to the other techniques. To closely examine this technique the terms of the integrated boundary layer equation 10 are plotted in figure 5 for both a ZPG flow and a FPG flow at approximately the same downstream location. The solid line, representing the sum of all the terms is fairly constant, indicating that the method has worked successfully for these two flows since τ_w/ρ is expected to be constant throughout the layer. The convection terms (term 3 from equation 10) change significantly between the ZPG and FPG flows. In the ZPG flow term 3 is positive and balances with the Reynolds shear stresses. However for the FPG flow term 3 is negative which balances the stronger pressure gradient term (term 6).

In figure 6, the effect of the pressure gradient on the skin friction coefficient can be seen for the different cases of Cal et al (2005). When comparing S-FPG 1 (3.5^o plate angle) to S-FPG 4 (15^o plate angle), the values of skin friction increase, while the Reynolds number decreases. This same trend is also seen when comparing S-CJ 2 (ZPG flow) to the other pressure gradient flows. However, there is little difference between the skin friction values of S-FPG 1 and S-FPG 3. As S-FPG 1, 2 and 3 develop downstream, the pressure gradient increases, as does the skin friction. For the strongest pressure gradient, S-FPG 4, (15^o plate angle), the skin friction coefficient is higher over the entire test section compared to the ZPG curve. In addition, the extreme angle actually imparts a strong enough pressure gradient to reduce the height of the momentum thickness. In each of the pressure gradient cases, the Reynolds number approaches a constant value due to the tendency of the momentum thickness to decrease while the freestream velocity increases.

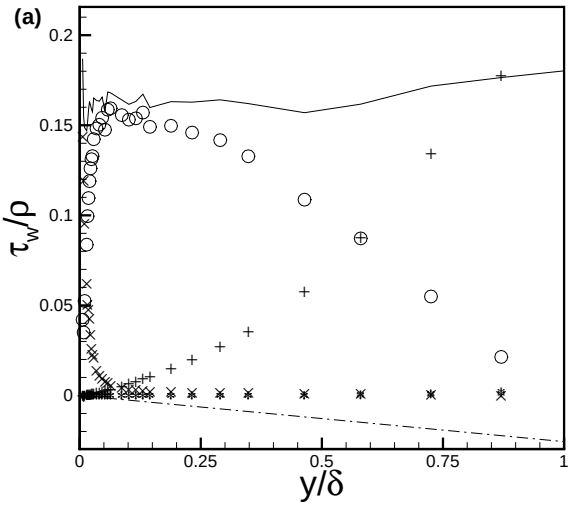

a) Integrated BL eqn for ZPG

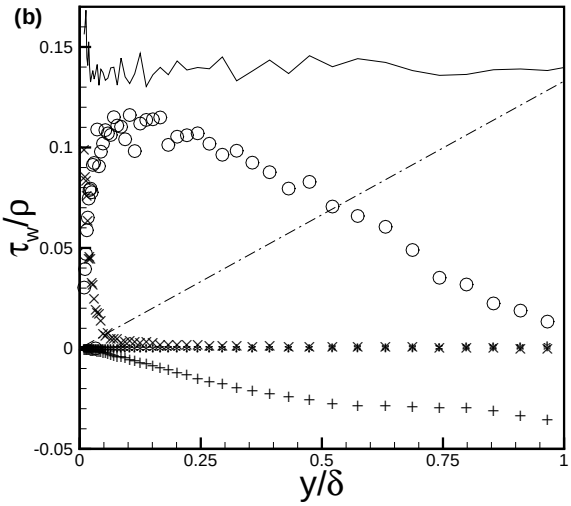

b) Integrated BL eqn for FPG

Fig. 5 Terms from the integrated momentum equation. $\times$: $\nu\frac{\partial \overline{U}}{\partial y}$, $\circ$: $\overline{uv}$, $+$:mean convection, $*$:Reynolds stresses, $- \cdot -$: $U_\infty \frac{\partial U_\infty}{\partial x}$, $-$:sum

The integrated boundary layer technique is good to use when there is less knowledge about the inner flow. However, problems arise with this method when there is not enough downstream locations placed close enough together such that accurate derivatives in the x-direction can be evaluated. In order to use this method, experiments would need to be designed with this in mind. Those experiments where windtunnel speeds change significantly downstream (such as strong pressure gradients), the measurement locations would need to be placed closer together to

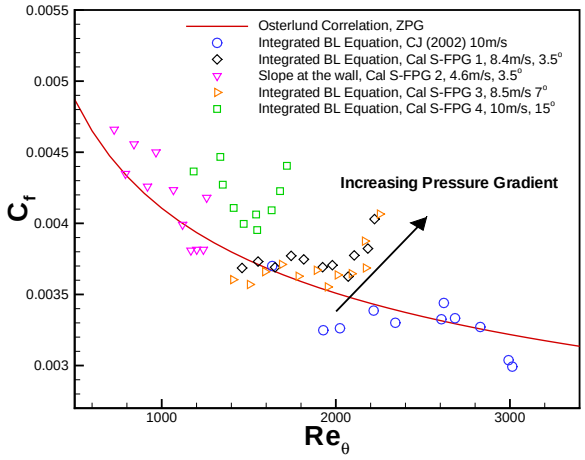

Fig. 6 Effect of pressure gradient strength on the value of C_f

capture the x-dependence. In addition, turning the wind-tunnel on and off during a downstream set of measurements will severely limit the accuracy of this method.

Inner Variables

In order to study the effects of the external pressure gradient and the upstream conditions on the inner flow, the mean velocity and Reynolds stresses are presented in inner variables. The friction velocity is the proper velocity scale in the inner region, (George and Castillo 1997) thus accurate values of u_* are needed for each profile. Based on the previous discussion, values of the friction velocity are obtained from the integrated momentum equation 10. They are used to scale all the FPG profiles in inner variables while the results from the Österlund correlation will be used for the ZPG profiles. It should be noted that for the flow of Cal (S-FPG 1-4) only 6 profiles are used where it is believed the skin friction has been computed most accurately. These locations are towards the back of the test section where the pressure gradient is largest.

The ZPG velocity profiles in inner variables are shown in figure 7(a) along with the ZPG data of Österlund and the hot-wire measurements of Smith and Smits (1995). As can be seen despite the large range in Reynolds numbers and wind-tunnel speeds the profiles tend to collapse in the inner region and overlap region as would be expected. Also, notice that as the Reynolds number increases, the overlap region gets longer.

The velocity profiles for the FPG cases of Cal et al. are shown in figure 7(b). The effect of the pressure gradient is not seen below $y^+ \approx 40$, as all four cases (S-FPG 1-4) collapse. However, in the overlap region, as the pressure gradient increases, there is a very minimal downward shift of the profiles. This shift is seen when comparing S-FPG 3 to S-FPG 4 in figure 7. Measurements closer than $y^+ \approx 15$ could not be obtained therefore the very near wall behavior could not be investigated for the strong FPG case.

In an effort to isolate the effect of the pressure gradient, profiles at a fixed Reynolds number of $\delta^+ \approx 380$ are selected from each case and plotted in figure 7(c) and figure 10. For the cases at 5 m/s, these profiles occur farther downstream than the 10 m/s cases. For the FPG flows, the selected profile for S-FPG 2 (5 m/s) has a stronger pressure gradient strength then the profiles selected for S-FPG 1 and S-FPG 3. At 10m/s, the profiles are closer to the leading edge where there is almost a negligible pressure gradient. Therefore there is a different strength of pressure gradient between the ZPG data, S-FPG 2 and S-FPG 4. Even with this difference in pressure gradient strength, all the profiles collapse through the overlap region until $y^+ \approx 100$.

The streamwise Reynolds stress component for the ZPG flows is scaled with the friction velocity, and plotted in figure 8(a). The different wind-tunnel speeds ($U_o = 5$, 10 and 20m/s) collapse up to $y^+ \approx 10$ where the peak in the Reynolds stress occurs. From this point on, each case collapses to its own curve, thereby removing the Reynolds number dependence. However, each wind-tunnel speed has its own curve indicating the dependence on the external conditions is apparent in the outer portion of the flow, but not the inner. The wall-normal Reynolds stress component (figure 8(b)) exhibits a similar trend. The collapse is extended farther from the wall, up to $y^+ \approx 100$, at which point the three cases depart, collapsing onto their own curves. The Reynolds shear stress (figure 8(c)) also collapses up to $y^+ \approx 100$, but the collapse is not as tight as the other two Reynolds stresses. Again, the effects of the external conditions, but not Reynolds number can be seen in the outer portion of the flow. Equation 7 is used to compute the value of the Reynolds shear stress from the gradient of the velocity. This theoretical profile matches the experimental data up to $y^+ \approx 100$, which is where the effects of the external conditions begin to appear. This is already well into the outer flow as $y/\delta_{95} = 0.1$ at $y^+ = 80$ and the equation is only expected to be valid in the inner flow.

For the FPG flows of Cal et al. the effect of Reynolds number and pressure gradient is explored in figure 9. Figure 9(a) shows the streamwise component $< u^2 >$ and the profiles for S-FPG 1, S-FPG 2 and S-FPG 3 tend to collapse throughout most of the boundary layer since the Reynolds number is very similar. However, most of the variations that are seen are due to the external pressure gradient. Another observation is that for the stronger pressure gradient, the profiles throughout the entire boundary layer change shape. This is seen for the profiles of case S-FPG 4 which has a plate angle of 15^o in addition to case S-FPG 3 with a 7^o plate angle.

The wall normal component, $< v^2 >$, plotted in figure 9(b), shows a much stronger influence of the pressure gradient. Although for $y^+ < 20$, the pressure

gradient does not seem to penetrate the inner boundary layer, the fluctuations are suppressed more as the strength of the pressure gradient increases. This is a direct result of the imposed pressure gradient and extends into the outer flow for $y^+ > 20$. For the the mild pressure gradient cases (S-FPG 1-3), this component is damped by approximately 20%. For the very strong pressure gradient case, the collapse of the inner region is hard to detect, since near-wall measurements were unable to be obtained. However, the wall-normal fluctuations are dampened as much as 30%, significantly more than the milder FPG cases. In addition, the overall shape of the profiles change indicating a possible approach towards quasi-laminarization (Cal 2006).

The Reynolds shear stress, $< -uv >$, is shown in figure 9(c) for the FPG data of Cal. This component behaves similarly to the $< v^2 >$ component. The profiles tend to collapse in the inner region for $y^+ < 20$, but show a strong effect of the pressure gradient further from the wall. In addition, as the pressure gradient increases the magnitude of this component decreases. The reduction of Reynolds shear stress is approximately 20% and 30% for the weak and strong pressure gradients, respectively. The theoretical profile for S-FPG 3 at $\delta^+ = 634$ is included in figure 9(c), and nearly matches that experimental data up to $y^+ \approx 70$. This is also the upper limit for the inner flow ($y/\delta_{95} = 0.1$) and thus the inner equation is no longer valid.

Reynolds stress profiles with the same Reynolds number of $\delta^+ = 370$, but different pressure gradient strengths are plotted in figure 10. The streamwise component $< u^2 >$ (figure 10(a)) shows a small dependence on wind-tunnel speed and pressure gradient strength. Both the wall normal Reynolds stress and the Reynolds shear stress show a much larger dependence on the pressure gradient. For the FPG measurements at 5m/s and for the very strong pressure gradient cases, there is a reduction of approximately 15% in the magnitude of the Reynolds stress throughout the entire boundary layer, where the values of λ^+ are 0.0028 and 0.0044, respectively. The strong pressure gradient (S-FPG 5, 15^o) reduces the $< v^2 >$ component significantly and thus decreases the $< uv >$ component. For the $< v^2 >$ component, this reduction is 26% and 44% for the $< uv >$ component. For S-FPG 3 (7^o plate angle), the reductions are 22% and 24% for the $< v^2 >$ and $< uv >$ respectively. It is also clear that variations in the profile due to pressure gradient exist for $y^+ < 15$, indicating its importance on the near wall Reynolds stress profiles.

Conclusion

Several techniques to compute the wall shear stress for various ZPG and FPG flows as well as the effects of upstream conditions and pressure gradient in the inner flow were investigated. In the absence of direct measurements using oil film interferometry, the integrated boundary layer equation is the most accurate method to use for pressure gradient flows. The momentum integral equation as well as the slope at the wall technique are difficult to implement experimentally unless accurate measurements are provided below $y^+ \approx 5$. For both the momentum integral equation and integrated boundary layer equation, the streamwise (x-direction) dependence of the velocity field is required. Although useful for ZPG flows, the Clauser method tends to break down in the presence of an external pressure gradient.

When the velocity profiles are plotted in inner similarity variables, the pressure gradient does not seem to affect the inner layer below $y^+ \approx 40$. However, the pressure gradient term contributed 5% of the momentum balance at $y^+ = 20$. The effect of external conditions such as upstream wind-tunnel speed and external pressure gradient appear in the outer, but not the inner region of the flow.

All three Reynolds stresses scaled with the friction velocity squared, collapsed in the inner region, but also showed the effects of wind-tunnel speed and external pressure gradient in the outer region of the flow. For the zero pressure gradient flows, the effects of Reynolds number were completely removed throughout the entire profile, thereby isolating the effect of upstream wind-tunnel speed. The external pressure gradient affected the flow above $y^+ \approx 20$, reducing both the $< v^2 >$ and the $< uv >$ components, as much as 30% for the strongest FPG flow.

Acknowledgements

Special thanks to Dr. Ronald Joslin from the office of Naval Research for supporting this work. Also, special thanks to Dr. Roosevelt Johnson from NSF-AGEP who allowed this international collaboration to be possible.

References

[1]Alving, A.E., Fernholz, H.H., 1995, "Turbulence measurements around a mild separation bubble and down-stream of reattachment," J. Fluid Mech., Vol. 322, pp. 279-328.

[2]Brown, J., and Naughton, J., "The Thin Oil Film Equation", NASA-TM 1999-208767, NASA Ames Research Center, March, 1999.

[3]Cal, R.B., "The Favorable Pressure Gradient Turbulent Boundary Layer," Ph.D. Thesis, Rensselaer Polytechnic Institute, Troy, NY, 2006.

[4]Cal, R.B., Johansson, T.G. and Castillo, L., "Initial Condition Effects on Turbulent Boundary Layers Subjected to Favorable Pressure Gradients," AIAA-2005-4812, 4th AIAA Theoretical Fluid Mechanics Conference, Toronto, Canada, 2005.

[5]Castillo, L., and Cal, R.B., "Evolution of the Favorable Pressure Gradient Turbulent Boundary Layer Towards a Quasi-Laminar State ," AIAA-2005-2883, 36th Fluid Dynamics Conference and Exhibut, San Francisco, CA, 2006.

[6]Castillo, L. and George, W.K., "Similarity Analysis for Turbulent Boundary Layer with Pressure Gradient: Outer Flow", AIAA Journal, Vol. 39 No. 1, pp 41-47, 2001.

[7]Castillo, L., and Johansson, G., "The effects of the upstream conditions on a low Reynolds number turbulent boundary layer with zero pressure gradient", Journal of Turbulence, 3, 031, 2002.

[8]Clauser, F.H.,"Turbulent Boundary Layers in Adverse Pressure Gradients", J.Aero.Sci., 21,1954.

[9]Fernholz, H. H., and Warnack, D., "The effects of a favorable pressure gadient and of the Reynolds number on an incompressible axisymmetric turbulent boundary layer. Part 1. The turbulent boundary layer", J. Fluid Mech., Vol. 359, pp. 329-356, 1998.

[10]George, W.K. and Castillo, L., "Zero-pressure gradient turbulent boundary layer", Appl. Mech. Rev 50, 689-729, 1997.

[11]Johansson, T.G. and Castillo, L., "Near-wall Measurements in Turbulent Boundary Layers using Laser Doppler Anemometry," Proc. FEDSM2002 - 31070, Montreal, Canada, 2002.

[12]Johansson, T.G., Mehdi, F., Shiri, F., and Naughton, J., "Skin Friction Measurements Using Oil Film Interferometry and Laser Doppler Anemometry," 35th AIAA Fluid Dynamics Conference and Exhibit, AIAA-2005-4673, Toronto, Canada, 2005.

[13]Nagib, H., Chauhan, K., Monkewitz, P., "Non-Universality of Karman Constant,"58th Annual Meeting of the American Physical Society, Division of Fluid Dynamics, APS Presentaion, Chicago, IL, 2005.

[14]Naughton, J., and Sheplak, M., "Modern Skin Friction Techniques: Description, Use, and What to do With the Data," 21st AIAA Advanced Measurement Technology and Ground Testing Conference, AIAA-2000-2521, Denver, CO, 2000.

[15]Naughton, J., and Sheplak, M., "Modern Developments in Shear Stress Measurement," Progress in Aerospace Sciences, Vol. 38, 515-570, 2002.

[16]Osterlund, J., "Experimental studies of zero pressure-gradient turbulent boundary layer flow", PhD Thesis, KTH, Stockholm, Sweden 1999.

[17]Österlund, J.M., Johansson, A., Nagib, H.M., and Hites, M.H., "Wall Shear Stress Measurements in High Reynolds number Boundary Layers from Two Facilities," 30th AIAA Fluid Dynamics Conference and Exhibit, AIAA-99-3814, Norfork, VA, 1999.

[18]Perry, A. E., "Turbulent boundary layers in decreasing adverse pressure gradients", J. Fluid Mech., Vol. 26, part 3, pp. 481-506, 1966.

[19]Preston, J.H., "The determination of turbulent skin friction by means of Pitot tubes", Journal of Royal Aeronautical Society, vol. 58, pp. 109-121, 1954.

[20]Schofield, W. H., "Equilibrium boundary layers in moderate to strong adverse pressure gradients", J. Fluid Mech., Vol 113, pp. 143-155, 1981.

[21]Smith, R.W., "Effect of Reynolds number on the structure of turbulent boundary layers", PhD Thesis, Princton Univ, 1994.

[22]Tanner, L., and Blows, L., "A study of the motion of oil films on surfaces in air flow, with applications to the measurement of skin friction", Journal of Physics E: Scientific Instrumentation, No. 3,9, pp. 194-202, 1976.

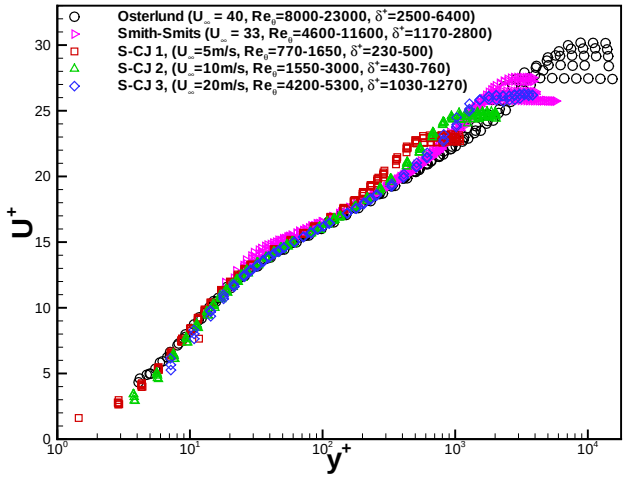

a) ZPG

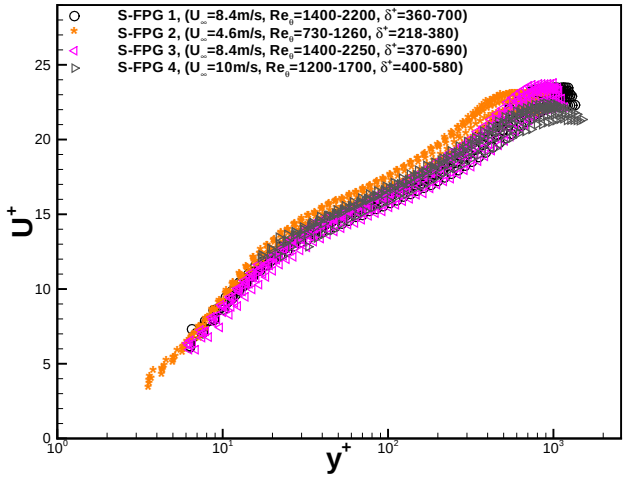

b) FPG

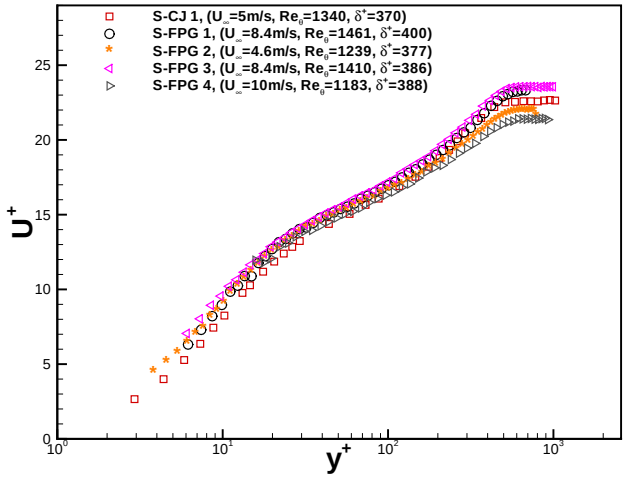

c) at fixed $\delta^+ = 370$

Fig. 7 Mean Velocity Profiles

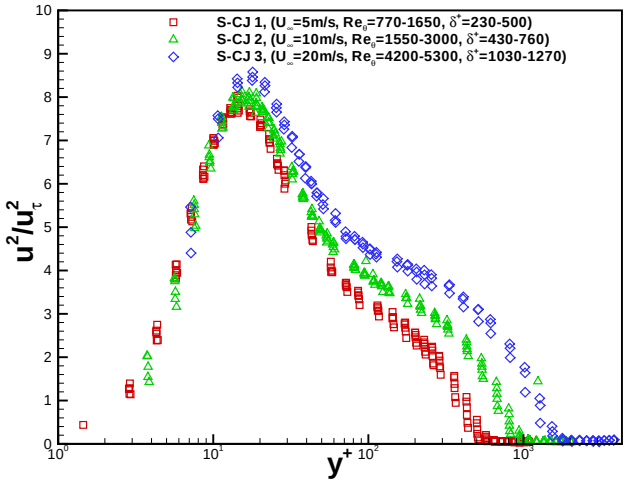

a) $\frac{<u'^2>}{u_\tau^2}$

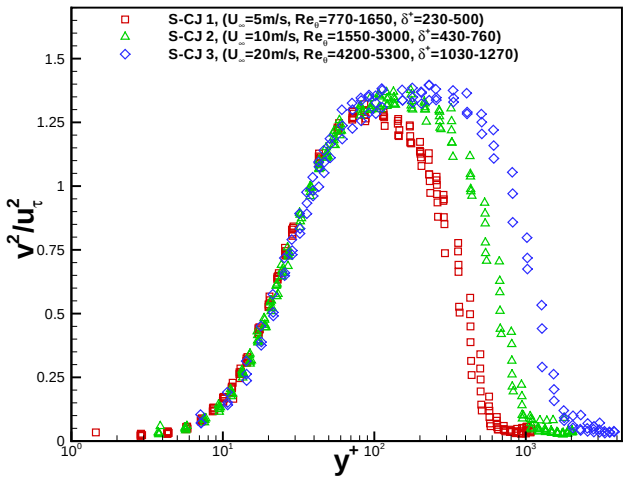

b) $\frac{<v'^2>}{u_\tau^2}$

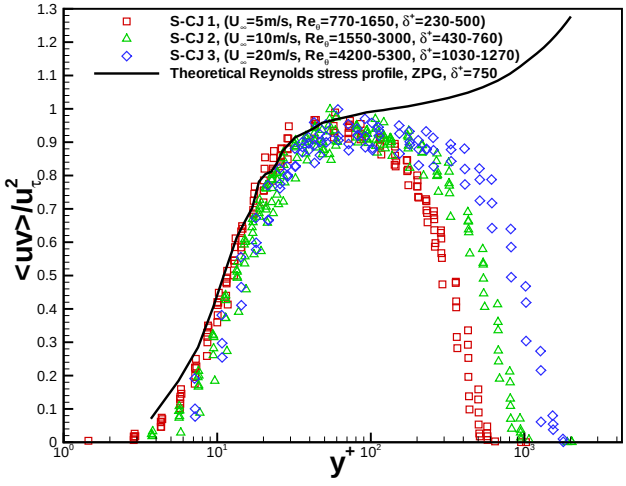

c) $\frac{<uv>}{u_\tau^2}$

Fig. 8 Reynolds stresses in inner variables for ZPG flows

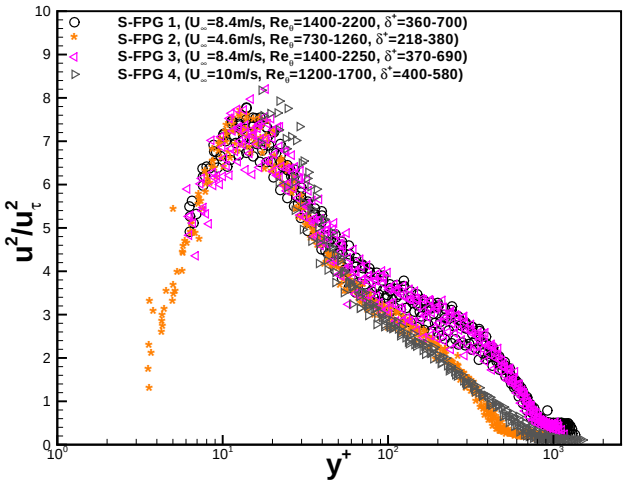

a) $\frac{<u'^2>}{u_\tau^2}$

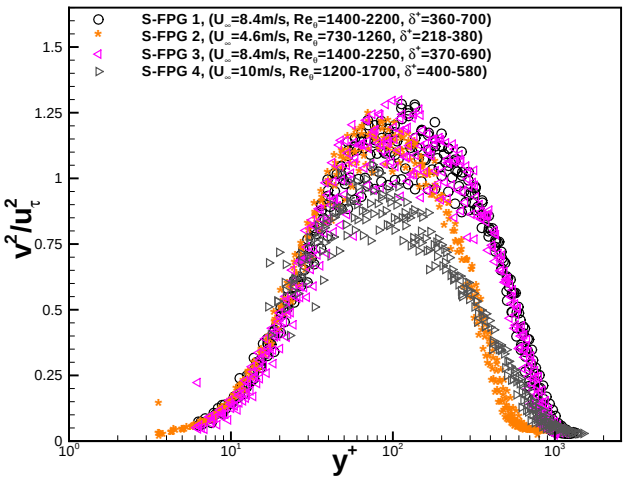

b) $\frac{<v'^2>}{u_\tau^2}$

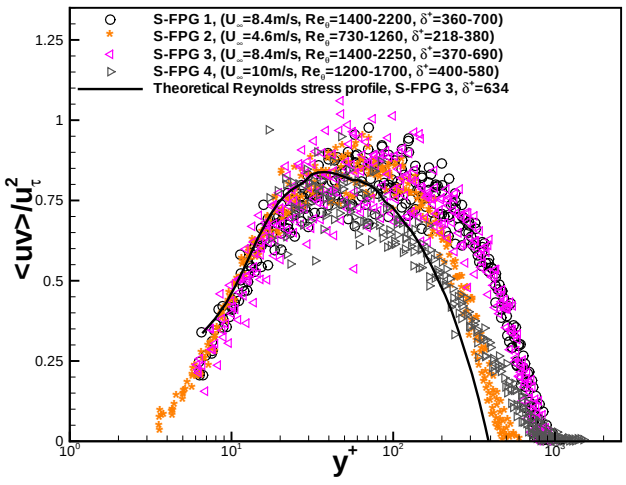

c) $\frac{<uv>}{u_\tau^2}$

Fig. 9 Reynolds stresses in inner variables for FPG flows

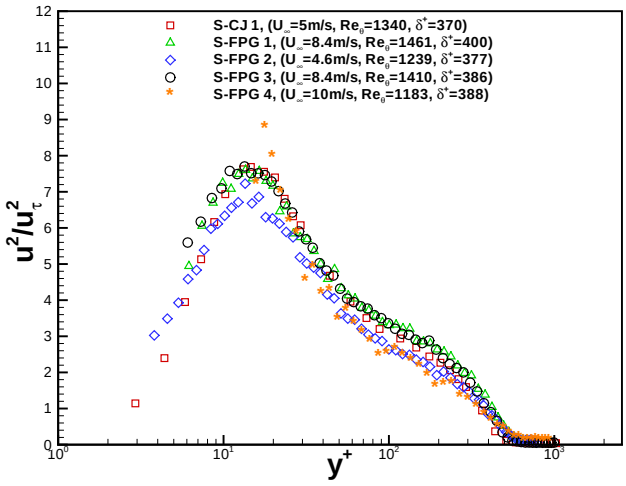

a) $\frac{<u'^2>}{u_\tau^2}$

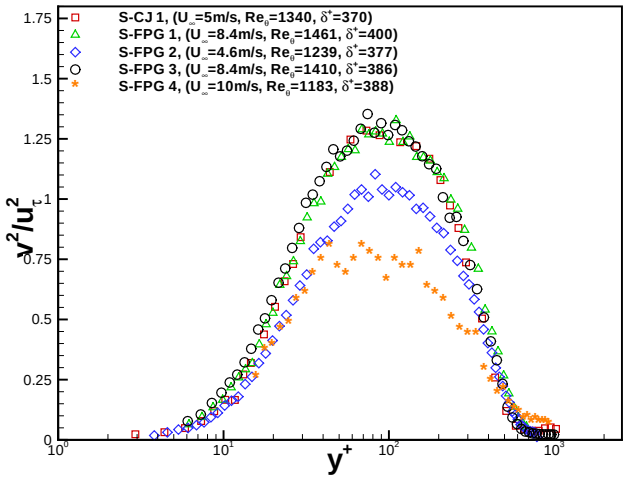

b) $\frac{<v'^2>}{u_\tau^2}$

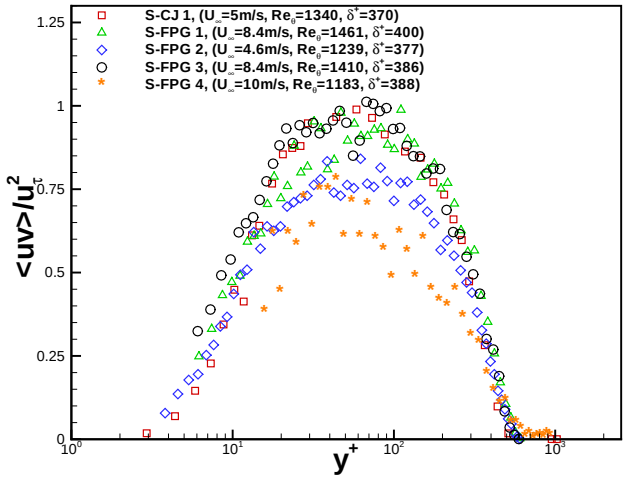

c) $\frac{<uv>}{u_\tau^2}$

Fig. 10 Reynolds stresses in inner variables at fixed $\delta^+ = 370$